

Disorder Limited Exciton Transport in Colloidal Single-Wall Carbon Nanotubes

Jared J. Crochet,^{*,†} Juan G. Duque,[†] James H. Werner,[‡] Brahim Lounis,^{§,||} Laurent Cognet,^{§,||} and Stephen K. Doorn^{*,‡}

[†]Physical Chemistry and Applied Spectroscopy, Los Alamos National Laboratory, New Mexico, United States

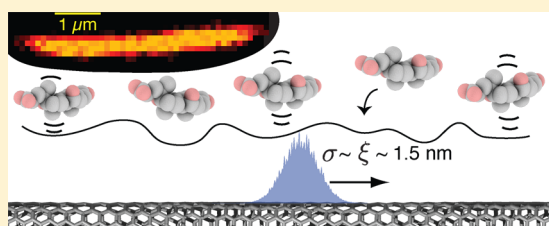
[‡]Center for Integrated Nanotechnologies, Los Alamos National Laboratory, New Mexico, United States

[§]Univ Bordeaux, LP2N, F-33405, Talence, France

^{||}CNRS, Institut d'Optique, LP2N, F-33405, Talence, France

ABSTRACT: We present measurements of S_1 exciton transport in (6,5) carbon nanotubes at room temperature in a colloidal environment. Exciton diffusion lengths associated with end quenching paired with photoluminescence lifetimes provide a direct basis for determining a median diffusion constant of approximately $7.5 \text{ cm}^2 \text{ s}^{-1}$. Our experimental results are compared to model diffusion constants calculated using a realistic exciton dispersion accounting for a logarithmic correction due to the exchange self-energy and a nonequilibrium distribution between bright and dark excitons. The intrinsic diffusion constant associated with acoustic phonon scattering is too large to explain the observed diffusion length, and as such, we attribute the observed transport to disorder-limited diffusional transport associated with the dynamics of the colloidal interface. In this model an effective surface potential limits the exciton mean free path to the same size as that of the exciton wave function, defined by the strength of the electron–hole Coulomb interaction.

KEYWORDS: Carbon nanotube, exciton, dephasing, transport, exchange interaction



Single-wall carbon nanotubes (SWNTs) are ideal models of infinite π orbital conjugation where the rigidity of the sp^2 lattice gives rise to nearly perfect one-dimensional conducting channels for charge carriers.¹ Moreover, semiconducting SWNTs provide a unique opportunity for photonics and optoelectronic applications because of well-defined optical resonances emanating from one-dimensional excitonic states.² The transport of energy in the form of excitons has implications in photovoltaics where both intra- and intertube transport are important factors in determining device performance.³ There have been several investigations aimed at determining room temperature intratube exciton diffusion lengths l_D in SWNTs with the consensus that on average $l_D > 100 \text{ nm}$,^{4–10} depending on the wrapping surfactant. Indeed, as shown by Siitonen et al.⁷ and Gokus et al.,¹¹ both l_D and the effective fluorescence lifetimes τ_{PL} can vary significantly for different environmental conditions. Moreover, the emission line-width of single tubes is also affected by environmental perturbations.^{12,13} Such behavior suggests that optical dephasing, exciton diffusion, and relaxation dynamics are largely tied to the local environment. Most importantly, knowledge of the intricacies of exciton diffusion is crucial for understanding photoexcited energy transport in the context of nanoscale optoelectronics.

With diffusional processes dominating the photophysics of carbon nanotubes, we set out to experimentally determine the exciton diffusion constant in (6,5) SWNTs. To avoid ambiguities associated with fluorescence quenching ranges

because of localized and delocalized electronic impurities,¹⁰ we determined the diffusion lengths directly from exciton quenching associated with the nanotube ends. This ability to directly probe behaviors previously accessed only indirectly is accomplished by imaging long, bright, and stable nanotube emitters at the diffraction limit. Paired with other recent reports,^{10–13} our results highlight the importance of such samples for accessing behaviors typically masked in measurements of shorter and more highly defected tubes. We found that for the (6,5) nanotube the median diffusion length was $l_D = 203 \pm 60 \text{ nm}$, and consistent with previous measurements,¹¹ the median effective fluorescence lifetime extracted from a biexponential decay was $\tau_{PL} = 55 \pm 4 \text{ ps}$. This corresponds to a median exciton diffusion constant of $D = 7.5 \pm 2.3 \text{ cm}^2 \text{ s}^{-1}$. Our experimentally obtained diffusion constant is examined against diffusion constants calculated within models of nonequilibrium band mediated transport initiated by acoustic phonons versus a mechanism mediated by disordered interface scattering.

Two samples of HiPco synthesized nanotubes (batch no. 187.4) were suspended in 1% aqueous deoxycholate (DOC) by shear mixing. Unsolubilized material was removed from the suspension by benchtop centrifugation. Imaging was performed on one sample with an inverted microscope equipped with an

Received: May 8, 2012

Revised: September 12, 2012

Published: September 17, 2012

electron-multiplying CCD camera (Princeton Instruments ProEm) and a 1.49 NA 60× objective in a wide field geometry, where the total detection efficiency was estimated to be $\approx 1.3\%$. The excitation source consisted of a continuous-wave solid-state 561 nm laser diode where the photon flux density was kept at $7 \times 10^{20} \text{ cm}^{-2} \text{ s}^{-1}$. This excitation is slightly off resonant from the S_2 maximum of the (6,5) tube, and we can expect a reduction of the absorption cross section per atom by $\approx 30\%$ from $1 \times 10^{-17} \text{ cm}^2$ to $7 \times 10^{-18} \text{ cm}^2$.¹⁴ Spectroscopy and lifetime measurements were carried out on the other sample of SWNTs that was immobilized in aqueous agarose gels (5 wt %). The dispersion was sandwiched between a glass coverslip and a glass slide and excited confocally at 567 nm with a dye laser which is resonant with S_2 of the (6,5) tube. The luminescence was sent to a cryogenically cooled 1D InGaAs detector (OMA V, Roper Scientific) placed at the output of a spectrometer. Lifetime measurements were carried out with confocal excitation at 567 nm using a femtosecond optical parametric oscillator, and the luminescence decays were recorded using conventional time-resolved single-photon counting.

Figure 1a shows a photoluminescence image of an approximately 6 μm SWNT. The PL image was uniform over

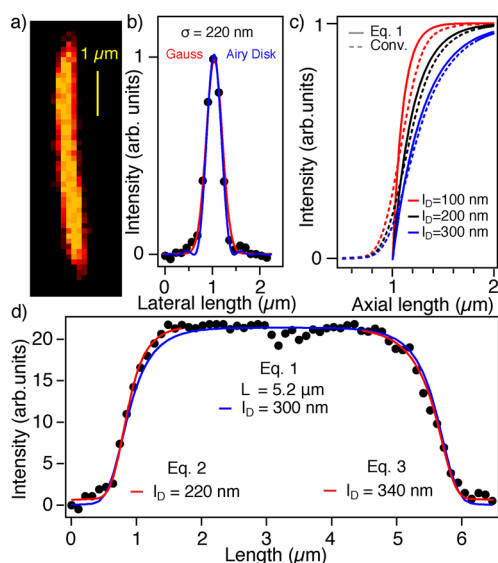


Figure 1. (a) Wide field photoluminescence image of an immobilized colloidal (6,5) nanotube. (b) Intensity cross-section perpendicular to the tube axis (black circles) from the image in part a with both Gaussian (red) and Airy disk (blue) fits. The Airy disk fit was for $\lambda = 986 \text{ nm}$ and $NA = 1.49$. This is the imaging point spread function (PSF). (c) Simulations of the fluorescence intensity at the end of the tube for various l_D (solid lines) and convolved with the PSF (dashed lines). This illustrates the ability to resolve varying diffusion lengths within our experimental spatial resolution. (d) Axial intensity cross-section (black circles) from part a where the fit (red and blue) is the solution of the 1D diffusion equation for different boundary conditions described in the text (eqs 1–3) convolved with the Airy disk in part b.

the length of the tube and did not show any signs of blinking or quenching except at the tube ends. The quantum yield of this particular tube was estimated to be a few percent using the corrected photon count rate from the camera, the exposure time, and the corrected absorption cross section stated earlier. The point spread function PSF of our microscope was determined by fitting the intensity profile perpendicular to

the tube axis in Figure 1a with either a Gaussian of width $\sigma = 220 \text{ nm}$ or a slice of an Airy disk which describes the diffraction limit. Using the numerical aperture of the objective $NA = 1.49$ and the wavelength of the emitted light $\lambda = 986 \text{ nm}$ we found a nearly perfect fit to the lateral intensity trace in Figure 1b with the Airy disk, indicating a diffraction limited image.

From this point forward we discuss the diffusive behavior of excitons in nanotubes where their concentration is low, given by our excitation rate of a few excitons per nanosecond. In this regime exciton–exciton interactions are negligible. If the excitons are truly behaving as one-dimensional diffusers such that the tube ends completely quench the fluorescence and the lifetime distribution of the excitons can be approximated by a single exponential $e^{-t/\tau_{PL}}$, the axial intensity is then given by the solution to the time-independent one-dimensional diffusion equation $Dc'' = -c/\tau_{PL} + S$. Here, c is the exciton concentration, S is the excitation rate, D is the exciton diffusion constant, τ_{PL} is the effective exciton lifetime, and the double prime is the Laplacian. With the boundary conditions $c(x \leq 0) = c(x \geq L) = 0$ and the emission intensity is uniform across the tube length as well as proportional to the steady-state exciton concentration, given by $S\tau_{PL}$, the solution takes the form,

$$c(x) = \left[1 - \frac{\sinh(x/l_D) + \sinh[(L-x)/l_D]}{\sinh(L/l_D)} \right] \quad (1)$$

where L is the length of the tube, $l_D = (D\tau_{PL})^{1/2}$ is the exciton diffusion length, and $S\tau_{PL}$ is set to unity which normalizes the equation. We tested the feasibility of using eq 1 convolved with the PSF to discern different diffusion lengths by simulating the expected response for various l_D 's, as in Figure 1c. We found we could clearly make a distinction between l_D varying by $\pm 50 \text{ nm}$. As an example of the fitting process applied to our experimental data for a tube with uniform brightness, we obtain a good fit to the axial trace of the tube shown in Figure 1a with $l_D = 300 \text{ nm}$ and $L = 5.2 \mu\text{m}$, as in Figure 1d. However, the realistic situation is where tubes are not uniformly emitting and each end has a slightly different environment which would result in different exciton transport properties. In this case the boundary condition for a half space must be used, that is, $c(x \leq 0) = 0$ and $c(x > 0) = S\tau_{PL}$ for the left end and $c(x < L) = S\tau_{PL}$ and $c(x \geq L) = 0$ for the right end of the tube. The normalized ($S\tau_{PL} = 1$) solution to the diffusion equation then becomes,

$$c(x) = \left[1 - \frac{\sinh[(L-x)/l_D]}{\sinh(L/l_D)} \right] \quad (2)$$

for the left end of the tube and

$$c(x) = \left[1 - \frac{\sinh(x/l_D)}{\sinh(L/l_D)} \right] \quad (3)$$

for the right end of the tube. In Figure 1d we show the comparison of using eqs 1–3, and we obtain $l_D = 220 \text{ nm}$ for the left end and $l_D = 340 \text{ nm}$ for the right end of the tube. A better fit to the intensity decays is obtained if each end of the tube is fit independently. This is evidenced by the fact a distribution of diffusion lengths is needed to fit all of the tubes and each tube end (Figure 2b). As a complement to the simulated intensity data in Figure 1c, we demonstrate for our experimental data the ability to discriminate between differing l_D 's in Figure 2a.

We examined end quenching from 55 tubes by using eqs 2 and 3 to find a median l_D that can represent an ensemble of

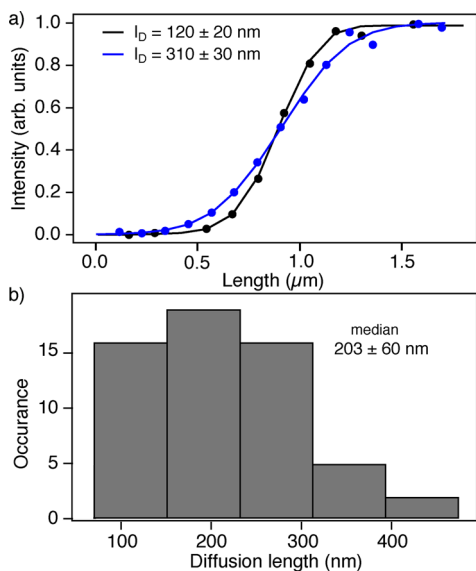


Figure 2. (a) Axial intensity traces from the ends of two different (6,5) SWNTs and fits using eq 2 for l_D . The data were horizontally scaled such that an intensity of 0.5 was at the same x -position. (b) Histogram of diffusion lengths for 59 tubes. A median diffusion length of $l_D \approx 203 \pm 60$ nm was determined.

tubes. The diffusion length was found to vary from tube-to-tube, and a histogram of all determined l_D 's is shown in Figure 2b and was found to have a median of $l_D \approx 203 \pm 60$ nm. Here the histogram bin width was chosen such that the integrated mean squared error was minimized.¹⁵ This result is consistent with single molecule stepwise quenching experiments for the same encapsulating surfactant,⁷ which not only provides validity to extracting l_D from stepwise quenching but also suggests that l_D may be independent of the quenching mechanism for localized electronic impurities such as midgap states or tube ends.¹⁰ Moreover, our result is nearly the same as the diffusion length of excitons in larger diameter tubes in laboratory air,¹⁶ which suggests excitons may experience a similar transport mechanism in atmospheric environments where several monolayers of adsorbates are present.

In Figure 3a we show a fluorescence lifetime for a single (6,5) tube with its associated fit. The time dependence of the fluorescence intensity is systematically biexponential and fit by $I(t) = (Ae^{-t/\tau_1} + Be^{-t/\tau_2})$ convoluted with the instrument response function (IRF) of the time-correlated single photon counting system.^{11,14} As reported previously,^{11,14} the long component τ_2 with a weight of $B\tau_2/(A\tau_1 + B\tau_2)$ accounts for $\approx 10\%$ of the total fluorescence intensity. The effective fluorescence lifetime was then calculated as a weighted average $\tau_{PL} = \int I(t)dt = (A\tau_1 + B\tau_2)/(A + B)$ and represents the effective bright exciton lifetime.¹⁴ In Figure 3b a histogram of τ_{PL} 's collected from 17 (6,5) tubes is shown. A median τ_{PL} of 55 ± 4 ps was deduced, and the diffusion constant, $D = l_D^2/\tau_{PL}$, was determined to be $D = 7.5 \pm 2.3$ cm² s⁻¹. This is in fair agreement with indirect measurements using a diffusion limited contact quenching model applied to fluorescence lifetimes and intensities of length sorted (6,5) tubes.⁸ Moreover, when compared to other indirect determinations of the diffusion constant,^{5,7,16} we find good agreements with our result if an accurately measured τ_{PL} , appropriate to the specific system under study, is applied. For example, the original result of ref 5 ($D = 0.4$ cm² s⁻¹) concerned sodium dodecyl benzene sulfonate

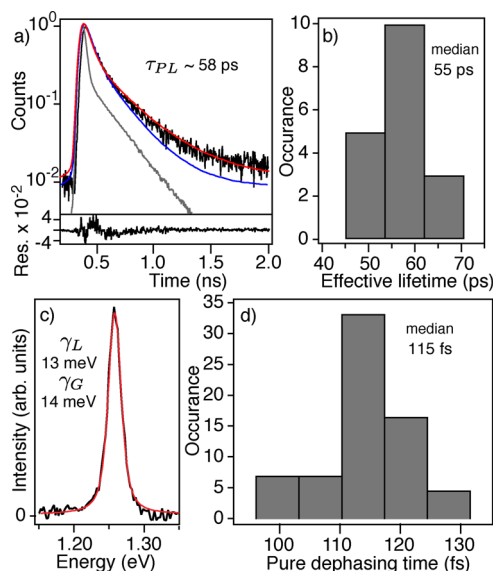


Figure 3. (a) Photoluminescence lifetime from a single (6,5) tube (black), instrument response function (gray), and double exponential (red) and monoexponential fits (blue). The double exponential fit is used to determine the effective fluorescence lifetime, τ_{PL} , where $\tau_1 \approx 49$ ps and $\tau_2 \approx 449$ ps. The residual of the double exponential fit is shown at the bottom of 3a and we consistently find that $\approx 90\%$ of the intensity is comprised of the fast component. The monoexponential fit has a time constant of $\tau \approx 58$ ps. (b) Histogram of effective lifetimes τ_{PL} where the median is $\tau_1 = 55 \pm 4$ ps. For details see Gokus et al.¹¹ (c) Fluorescence spectrum from a single (6,5) tube (black) and a Voigt fit (red) used to determine the pure dephasing time, τ_ϕ , from the Lorentzian component γ_L . The inhomogeneous broadening is given by the Gaussian component γ_G . The errors in the linewidths are less than 1%. (d) Histogram of pure dephasing times calculated from the line width $\gamma_L = 2\hbar\tau_\phi^{-1}$. The median is $\tau_\phi = 115$ fs.

(SDBS) dispersed nanotubes and relied on the use of a τ_{PL} of 100 ps, originally estimated as a median value from several literature results.⁵ If instead a more current value for τ_{PL} of 53 ps in SDBS¹⁴ is used, and by accounting for the effect of different surfactant environments (SDBS vs our use of DOC),⁷ a comparable D of 5.4 cm² s⁻¹ results. Similarly, indirect determinations of $D = 2.8$ cm² s⁻¹ (in DOC)⁷ and of 4.7 cm² s⁻¹ (for individual tubes suspended in air)¹⁶ result from τ_{PL} of 50 ps^{11,12} and 85 ps,¹⁷ respectively, obtained from similar sample types. These indirect determinations are thus seen to be in good agreement with our direct evaluation of D .

With this directly obtained diffusion constant we now investigate the fluorescence line width, which contains information about the exciton dephasing mechanism. Exciton dephasing, which drives transport by changing the momentum and consequently the group velocity of the exciton, should vary significantly for different environments. Indeed, recent time-resolved coherent spectroscopies of (6,5) nanotubes in various matrices have shown that this is the case.¹⁸

The fluorescence line width at the single tube level, given by $\Gamma = \hbar[\tau_{PL}^{-1} + 2\tau_\phi^{-1}]$, where τ_{PL} is the effective lifetime or population decay and τ_ϕ is the pure dephasing time describing the mean free time between decohering scattering events, was recently found to vary linearly over a wide range of temperatures in vacuum.¹⁹ This was attributed to a small amount of constant environmental dephasing of $\Gamma_0 \approx 2$ meV and an exciton-acoustic phonon coupling term that lead to a diameter-dependent Γ . In comparison, in Figure 3c we show an

emission spectrum for a single (6,5) tube with its associated Voigt fit as described by Cambre et al.¹³ and find that the Gaussian component, inhomogeneous broadening, has a width of $\gamma_G \approx 14$ meV and the Lorentzian component, homogeneous broadening, has a width of $\gamma_L \approx 13$ meV. We note that a pure Lorentzian line shape gives an approximate 20% increase in the root-mean-square error associated with the fit. This is consistent with the values obtained from a similar synthesis batch of (6,4) tubes¹³ and suggests that inhomogeneous broadening due to environmental dephasing may be significant in the colloidal environment. In Figure 3b a histogram of pure exciton dephasing times calculated from several Lorentzian components of the emission linewidths is shown: $\tau_\phi = 2\hbar/\gamma_L$. The median was found to be $\tau_\phi = 115$ fs and is very similar to that found for the same diameter of tubes suspended over trenches,¹⁹ where inhomogeneous broadening is expected to be less significant. Interestingly, it was found that for colloidal tubes from the same synthesis batch, the emission intensity varied significantly for tubes suspended in two different surfactant systems, while Γ was nearly unchanged.¹² Only for highly defective tubes was Γ shown to change significantly and attributed to additional lattice defect dephasing. However, the large spread in the data and the significant increase in inhomogeneous broadening on going from vacuum suggests local environmental fluctuations at room temperature introduce a significant degree of disorder as expected from the dynamic nature of the colloidal interface. Pairing the pure dephasing time with our experimentally determined diffusion constant allows us to address the possible mechanisms behind exciton diffusion in colloidal nanotubes. We proceed to quantify the transport mechanism in (6,5) nanotubes using what is known about the band structure and bright and dark exciton scattering.

In chiral carbon nanotubes there are two distinct A line group symmetry excitons split by an exchange energy of $\Delta \approx 5$ meV that have even A_2 and odd parity A_1 .^{20,21} The higher energy A_1 exciton carries all of the oscillator strength and therefore is optically bright, while the lower energy A_2 exciton is dark. It is also known that the bright exciton dispersion $\epsilon_{b,q}$ which dictates transport properties through the group velocity, is nonparabolic because of the exchange interaction and varies as $\epsilon_{b,q} = \alpha q^2 \log(q_0/|q|)$, where q_0 is a momentum cutoff, q is the center of mass momentum, and α is a coupling constant that measures the strength of the exchange energy.^{20,22} Here $\epsilon_{b,q}$ is singular at $q = 0$; however the singularity is removable as $\lim_{q \rightarrow 0} \epsilon_{b,q} = 0$. Therefore, the diffusion constant of excitons in SWNTs should be treated carefully since the effective mass has a singular logarithmic correction as $q \rightarrow 0$. Recently this behavior has been explained in terms of the spin-charge velocity separation aspect of the Luttinger liquid²³ and has roots in the quasi-particle renormalization of the graphene dispersion which does not exactly cancel in one-dimension.²⁴ We find the parameters α and q_0 by fitting $\epsilon_{b,q}$ to the thermally accessible momentum states by the predictions of Jiang et al. for the (6,5) tube calculated using the Bethe-Salpeter equation:²⁰ $\alpha = 2.85$ eV nm² and $q_0 = 1.4$ nm⁻¹. The dark exciton, however, has a dispersion of a free particle, $\epsilon_{d,q} = \hbar^2 q^2 / 2m^*$, with an effective mass given by $m^* \approx 1.5(m_e^* + m_h^*)$ where m_e^* and m_h^* are the effective masses of the electron and hole.²² From this point forward, we take for the (6,5) tube $m_e^* + m_h^* = 0.29m_e$.²⁵ Both ϵ_d and ϵ_b are shown in Figure 4a where the bright state is scaled by the optical gap ϵ_g and the dark exciton scaled by $\epsilon_g - \Delta$.

It is also known that the A_2 and A_1 symmetry excitons can interparity scatter due to A line group symmetry breaking with

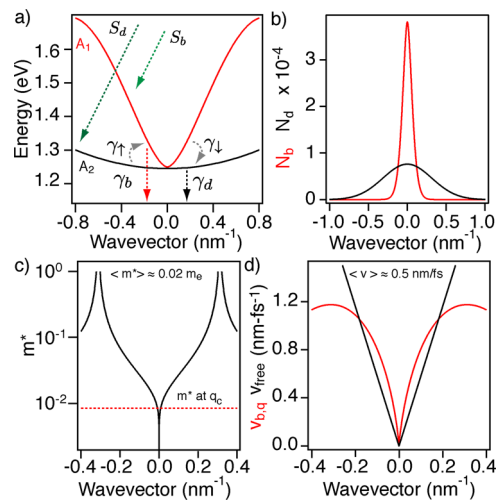


Figure 4. (a) Exciton dispersions used in the calculation of the diffusion constant. The bright A_1 symmetry exciton is shown in red, and the dark A_2 symmetry exciton is shown in black. The rates used to calculate the bright exciton distribution are also shown, where γ_1 and γ_\uparrow are the A_1/A_2 interparity scattering, γ_b is the A_1 exciton decay dominated by nonradiative processes, γ_d is the A_2 exciton decay, and S_b/S_d represents A_1/A_2 exciton generation rates. (b) q dependent probability distribution functions calculated from intraband thermalization only. (c) q dependent bright exciton effective mass. The red dashed line illustrates the mass where the dispersion of light intersects the exciton band. (d) q dependent exciton velocities calculated with the exchange correction to the dispersion (red) and an effective mass exciton $m^* = 0.02m_e$ with a parabolic dispersion (black).

rates given by γ_\uparrow and γ_\downarrow ; however, this process is known to be slow when compared to the lifetimes of both parity excitons.^{11–14} Here $\gamma_\uparrow = \gamma_0 n(\Delta)$ and $\gamma_\downarrow = \gamma_0 [n(\Delta) + 1]$, where n is the Bose–Einstein distribution function and γ_0 is the zero temperature scattering rate. For small γ_0 compared to other decay processes this behavior results in a nonequilibrium distribution between the states largely responsible for the biexponential behavior shown in Figure 3a^{11,13} and has also been shown directly by low-temperature photoluminescence spectroscopy at the single tube²⁶ and ensemble levels.²⁷ To account for the distribution between A_1 and A_2 excitons as well as other processes including: the generation S_b and effective decay γ_b of A_1 excitons, and the generation S_d and effective decay γ_d of A_2 excitons; the population of the bright state at $q = 0$ is calculated by the steady state solution to the system in Figure 4a such that,

$$n_b = \frac{\gamma_\uparrow S_d + (\gamma_d + \gamma_\uparrow) S_b}{\gamma_d \gamma_\downarrow + \gamma_d \gamma_b + \gamma_\uparrow \gamma_b} \quad (4)$$

Likewise, the lower energy A_2 exciton population becomes,

$$n_d = \frac{\gamma_\downarrow S_b + (\gamma_b + \gamma_\downarrow) S_d}{\gamma_d \gamma_\downarrow + \gamma_d \gamma_b + \gamma_\uparrow \gamma_b} \quad (5)$$

This allows us to define the total exciton fraction in the bright and dark states as $\eta_b = n_b / (n_b + n_d)$ and $\eta_d = n_d / (n_b + n_d)$. We calculated the populations in each state by assuming the exciton generation rates take the form $S_b = S_d$.¹¹ This is valid under low intensity or continuous wave excitation, the initial population of both states is equal upon internal conversion from higher lying excited states such as S_2 , and the exciton dephasing mechanism is much faster than any of the scattering mechanisms in Figure

4a, leading to a rapid intraband thermalization. Using parameters that describe the biexponential decay of the photoluminescence: $\gamma_d = 2 \text{ ns}^{-1}$, $\gamma_b = 20 \text{ ns}^{-1}$, and $\gamma_0 = 0.05 \text{ ns}^{-1}$,¹¹ we find at steady state the probability of finding an exciton in the bright state $\eta_b \approx 11\%$ is much smaller than the probability of finding an exciton within the dark state $\eta_d \approx 89\%$. Moreover, if we take $\gamma_0 = 0$ the probabilities become $\eta_b \approx 9\%$ and $\eta_d \approx 91\%$, which illustrates that the weak, but finite interband scattering results in an $\approx 2\%$ increase of the population of excitons in the bright state. Therefore, at room temperature interparity scattering has an insignificant effect on thermally averaged observables since at steady state $\approx 98\%$ of the bright excitons originated in the bright state and only $\approx 2\%$ come from the dark state. Within this argument, including only rapid intraband thermalization, we can define q dependent probability distribution functions of the excitons as $N_{i,q} = e^{-\beta \epsilon_{i,q}} / \sum_q e^{-\beta \epsilon_{i,q}}$, where $i = b$ or d and $\beta = k_b T$. In Figure 4b we show $N_{b,q}$ and $N_{d,q}$ calculated at room temperature. As a first implication of this model, from $N_{b,q}$ and the effective mass $m^* = \hbar^2 |(\partial^2 \epsilon_b) / (\partial q^2)|^{-1}$, we calculated the expected thermally averaged mass of bright excitons as $\langle m^* \rangle$, where $\langle \dots \rangle = \int_{-\infty}^{\infty} N_{b,q} \dots dq$, and find at room temperature $\langle m^* \rangle \approx 0.02 m_e$. This is an essential point because m^* itself is q dependent and $m^* \rightarrow 0$ as $q \rightarrow 0$, Figure 4c. Also the exciton mass at $\epsilon_{b,q}(q_c)$, where q_c is the wavevector where the dispersion of light intersects the exciton band, is significantly smaller than $\langle m^* \rangle$.

Next we investigated the mechanism of exciton transport by considering two different processes for exciton diffusion: transport by scattering with intrinsic phonons and disorder limited transport by interfacial scattering. In the first case, the transport is governed by the scattering of excitons within the band $\epsilon_{b,q}$ by low energy phonons such as acoustic phonons, Figure 5a. Here the diffusion constant can be calculated from the exciton group velocity,

$$v_{b,q} = \hbar^{-1} \frac{\partial \epsilon_{b,q}}{\partial q} \quad (6)$$

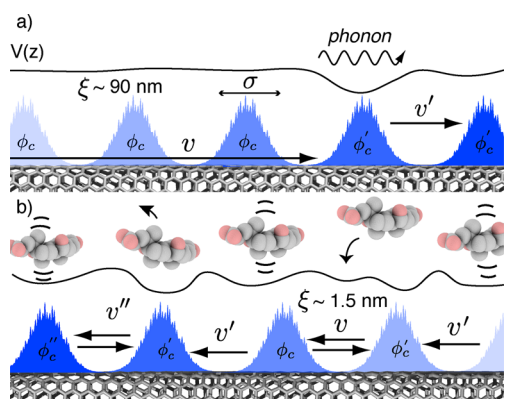


Figure 5. Schematic of exciton transport mechanisms in carbon nanotubes. (a) Intrinsic case where an exciton wave packet, described by a Gaussian electron–hole pair probability distribution of width σ , moves with a velocity v and scatters at a lattice site through the deformation potential where phonon absorption or emission takes place and changes the exciton velocity to v' . Within the coherence length ξ the phase of the wave function ϕ_c is preserved. (b) The disorder limited case where a dynamic, random surface potential $V(z)$ associated with the colloidal interface facilitates exciton scattering between energy minima spaced by an average distance that defines the coherence length ξ .

such that $D = \langle v_{b,q}^2 \tau_\phi \rangle$.²⁸ In Figure 4d we show $|v_{b,q}|$ for the logarithmically corrected dispersion compared to the velocity of a free particle $|v_{q,\text{free}}| = \hbar |q| / m^*$ with $m^* = 0.02 m_e$, and it is apparent how the velocity at small q is significantly increased because of the exchange self-energy. Also, we note that, in the limit of a single parabolic exciton band of constant mass m^* with q independent dephasing and a Boltzmann probability distribution function, the diffusion constant in this description gives the familiar result for a classical particle, $D = k_b T \tau_\phi / m^*$, which is often used for describing excitons in carbon nanotubes. However, we find that for the measured median exciton dephasing time and the logarithmically corrected dispersion $D \approx 370 \text{ cm}^2 \text{ s}^{-1}$. With this diffusion constant the corresponding mean free path, average distance traveled before a change in momentum or coherence length,²⁹ due to acoustic phonon scattering would be $\xi = (2D\tau_\phi)^{1/2} \approx 90 \text{ nm}$ and the diffusion length would be $l_D \approx 1400 \text{ nm}$. This diffusion length is larger than what we obtain experimentally and suggests this type of transport does not dominate in the colloidal environment.

Next, we examined the effects of interface scattering or a disordered environment on the diffusion constant. In this regime, an exciton wavepacket moves with a certain transport velocity v and is scattered by an inhomogeneous surface potential provided by the dynamic colloidal interface, Figure 5b. Such motion is derived from standard theory of waves propagating in strongly scattering media and is described by a mean free path ξ such that $D = v\xi$.³⁰ Here, the transport velocity is given by the thermally averaged group velocity $v = \langle |v_{b,q}| \rangle$, and at room temperature we find for the logarithmically corrected dispersion $v \approx 0.5 \text{ nm fs}^{-1}$. In order for $D \approx 7.5 \text{ cm}^2 \text{ s}^{-1}$ the mean free path must be $\xi \approx 1.5 \text{ nm}$. As a theoretical comparison, the predicted exciton correlation length, full width-half-maximum of the nearly Gaussian envelope function, of a (6,5) nanotube embedded in an effective dielectric constant of $\kappa = 1.85$ is $\sigma \approx 1.5 \text{ nm}$.³¹ Moreover, an experimentally determined exciton wave function with a Gaussian full-width half-maximum of $\sigma = 2 \pm 0.7 \text{ nm}$ has been measured by phase-space filling.³² This suggests that the exciton travels, on average, a distance equal to the width of a distribution function describing the probability to find an electron or hole at a fixed hole or electron position. Moreover, excitons are coupled to the local environment such that a scattering event can take place on average every distance ξ which gives an upper estimate to the linear packing density of the colloidal interface. In this description a larger diffusion constant would suggest a less disordered interface and may be experimentally tested by varying the surfactant composition and concentration.

In conclusion, we have measured the exciton diffusion constant in colloidal (6,5) carbon nanotubes by a combination of photoluminescence imaging and time-resolved fluorescence microscopies. The mean diffusion constant was found to be $D \approx 7.5 \text{ cm}^2 \text{ s}^{-1}$ and attributed to disorder limited exciton transport. The mean free path ξ we obtained suggests that the exciton moves a distance comparable to its electron–hole correlation length σ before scattering to a new velocity and supports an apparent diffusive “hopping” behavior of excitons in colloidal nanotubes. Moreover, our model of exciton transport accounts for what is known theoretically about excitons in carbon nanotubes beyond the simple classical particle picture, which ignores the exchange self-energy.²⁴ This work is also important for understanding the impact of the colloidal interface for the photophysics of carbon nanotubes for single molecule detection applications.¹⁰ For example, we point

out how the mobility of photoexcitations can be altered by effectively changing the surface potential experienced by the excitons and may allow for intrinsic transport. Such insight is of value for colloidal science where the excitons act as a surface probe, and we expect that, by tailoring the composition and structure of the interface, the tunability of the optical properties of carbon nanotubes can be realized.

AUTHOR INFORMATION

Corresponding Author

*E-mail: jcrochet@lanl.gov; skdoorn@lanl.gov.

Notes

The authors declare no competing financial interest.

ACKNOWLEDGMENTS

J.C. thanks Jay D. Sau for stimulating theoretical discussions. This work was performed, in part, at the Center for Integrated Nanotechnologies, a U.S. Department of Energy, Office of Basic Energy Sciences user facility and partially supported by LANL-LDRD program. Los Alamos National Laboratory is operated by Los Alamos National Security, LLC, for the National Nuclear Security Administration of the U.S. Department of Energy under contract DE-AC52-06NA25396. This work was also funded by the Agence Nationale de la Recherche, Région Aquitaine, the French Ministry of Education and Research, and the European Research Council.

REFERENCES

- (1) Avouris, P.; Appenzeller, J.; Martel, R.; Wind, S. P. *IEEE* **2003**, *91*, 1772–1784.
- (2) Jorio, A.; Dresselhaus, G.; Dresselhaus, M. *Carbon Nanotubes: Advanced Topics in the Synthesis, Structure, Properties and Applications*; Springer: New York, 2008.
- (3) Bindl, D. J.; Wu, M.-Y.; Prehn, F. C.; Arnold, M. S. *Nano Lett.* **2011**, *11*, 455–460.
- (4) Lefebvre, J.; Austing, D. G.; Bond, J.; Finnie, P. *Nano Lett.* **2006**, *6*, 1603–1608.
- (5) Cognet, L.; Tsyboulski, D. A.; Rocha, J.-D. R.; Doyle, C. D.; Tour, J. M.; Weisman, R. B. *Science* **2007**, *316*, 1465–1468.
- (6) Georgi, C.; Böhmeler, M.; Qian, H.; Novotny, L.; Hartschuh, A. *Phys. Status Solidi B* **2009**, *246*, 2683–2688.
- (7) Siitonen, A. J.; Tsyboulski, D. A.; Bachilo, S. M.; Weisman, R. B. *Nano Lett.* **2010**, *10*, 1595–1599.
- (8) Hertel, T.; Himmelein, S.; Ackermann, T.; Stich, D.; Crochet, J. *ACS Nano* **2010**, *4*, 7161–7168.
- (9) Moritsubo, S.; Murai, T.; Shimada, T.; Murakami, Y.; Chiashi, S.; Maruyama, S.; Kato, Y. K. *Phys. Rev. Lett.* **2010**, *104*, 247402.
- (10) Crochet, J. J.; Duque, J. G.; Werner, J. H.; Doorn, S. K. *Nat. Nanotechnol.* **2012**, *7*, 126–132.
- (11) Gokus, T.; Cognet, L.; Duque, J. G.; Pasquali, M.; Hartschuh, A.; Lounis, B. *J. Phys. Chem. C* **2010**, *114*, 14025–14028.
- (12) Duque, J. G.; Pasquali, M.; Cognet, L.; Lounis, B. *ACS Nano* **2009**, *3*, 2153–2156.
- (13) Cambré, S.; Santos, S. M.; Wenseleers, W.; Nugraha, A. R. T.; Saito, R.; Cognet, L.; Lounis, B. *ACS Nano* **2012**, *6*, 2649–2655.
- (14) Berciaud, S.; Cognet, L.; Lounis, B. *Phys. Rev. Lett.* **2008**, *101*, 077402.
- (15) Scott, D. W. *Biometrika* **1979**, *66*, 605–610.
- (16) Xie, J.; Inaba, T.; Sugiyama, R.; Homma, Y. *Phys. Rev. B* **2012**, *85*, 085434.
- (17) Xiao, Y.-F.; Nhan, T. Q.; Wilson, M. W. B.; Fraser, J. M. *Phys. Rev. Lett.* **2010**, *104*, 017401.
- (18) Graham, M. W.; Ma, Y.-Z.; Green, A. A.; Hersam, M. C.; Fleming, G. R. *J. Chem. Phys.* **2011**, *134*, 034504.
- (19) Yoshikawa, K.; Matsunaga, R.; Matsuda, K.; Kanemitsu, Y. *Appl. Phys. Lett.* **2009**, *94*, 093109.

- (20) Jiang, J.; Saito, R.; Samsonidze, G. G.; Jorio, A.; Chou, S. G.; Dresselhaus, G.; Dresselhaus, M. S. *Phys. Rev. B* **2007**, *75*, 035407.
- (21) Shaver, J.; Crooker, S. A.; Fagan, J. A.; Hobbie, E. K.; Ubrig, N.; Portugall, O.; Perebeinos, V.; Avouris, P.; Kono, J. *Phys. Rev. B* **2008**, *78*, 081402.
- (22) Perebeinos, V.; Tersoff, J.; Avouris, P. *Nano Lett.* **2005**, *5*, 2495–2499.
- (23) Konik, R. M. *Phys. Rev. Lett.* **2011**, *106*, 136805.
- (24) Kane, C. L.; Mele, E. J. *Phys. Rev. Lett.* **2004**, *93*, 197402.
- (25) Jorio, A.; Fantini, C.; Pimenta, M. A.; Capaz, R. B.; Samsonidze, G. G.; Dresselhaus, G.; Dresselhaus, M. S.; Jiang, J.; Kobayashi, N.; Grüneis, A.; Saito, R. *Phys. Rev. B* **2005**, *71*, 075401.
- (26) Matsunaga, R.; Miyauchi, Y.; Matsuda, K.; Kanemitsu, Y. *Phys. Rev. B* **2009**, *80*, 115436.
- (27) Duque, J. G.; Hamilton, C. E.; Gupta, G.; Crooker, S. A.; Crochet, J. J.; Mohite, A.; Htoon, H.; Obrey, K. A. D.; Dattelbaum, A. M.; Doorn, S. K. *ACS Nano* **2011**, *5*, 6686–6694.
- (28) Munn, R. W.; Siebrand, W. J. *J. Chem. Phys.* **1970**, *52*, 47–63.
- (29) Piryatinski, A.; Asher, S. A.; Mukamel, S. *J. Phys. Chem. A* **2002**, *106*, 3524–3530.
- (30) Agranovich, V. M.; Konobeev, Y. V. *Phys. Status Solidi B* **1968**, *27*, 435–442.
- (31) Capaz, R. B.; Spataru, C. D.; Ismail-Beigi, S.; Louie, S. G. *Phys. Rev. B* **2006**, *74*, 121401.
- (32) Lüer, L.; Hoseinkhani, S.; Polli, D.; Crochet, J.; Hertel, T.; Lanzani, G. *Nat. Phys.* **2009**, *5*, 54–58.